PCCP

PAPER

View Article Online
View Journal

Cite this: DOI: 10.1039/d5cp04576b

Spontaneous generation of hydrogen from water using modified dodecaborate ions

Hugo A. López Peña [a] and Puru Jena *[b]

Received 25th November 2025,
Accepted 26th February 2026

DOI: 10.1039/d5cp04576b

rsc.li/pccp

Efficient hydrogen production from water is a key requirement for a successful hydrogen economy. The dodecaborate anion $[B_{12}H_{12}]^{2-}$ and its derivatives $[B_{12}X_{12}]^{2-}$ (X = F, Cl, Br, I, CN), known for their enhanced stability, have catalytic potential for activating small molecules, such as NH_3, CO_2, and N_2, once a ligand is removed. In this work, we computationally explored the electronic structures of $[B_{12}X_n]^q$ (X = Br, I, CN; n = 11, 10; q = 2−, 1−, 0) and the thermodynamics of their interaction with water. We show that, among these, $[B_{12}X_{10}]^{-\bullet}$ (X = Br, I) are the most suitable for spontaneous hydrogen generation. A detailed description of the catalytic mechanism is presented.

1 Introduction

The rising global temperature caused by the burning of fossil fuels makes it imperative that the world switch to clean, affordable, and renewable energy sources. Hydrogen is a potential solution, as it produces water when burned. However, hydrogen is not an energy source, but an energy carrier, and must be produced. For a carbon-free world, it would be ideal if it could be produced efficiently from water. Water splitting is a non-spontaneous process that requires external energy to proceed. The Gibbs free energy to break one mole of water in the gas phase into molecular hydrogen and oxygen is approximately 2.37 eV at room temperature.[1] Thermodynamic parameters of any chemistry being proposed as part of a thermochemical cycle of hydrogen production directly impact operating conditions and hence the overall efficiency of the process.[2] Therefore, finding spontaneous or near spontaneous reactions capable of producing hydrogen is of great importance. In this paper, we explore the potential of dodecaborate anion derivatives to produce hydrogen *via* water splitting.

Dodecaborate anion, $[B_{12}H_{12}]^{2-}$, predicted in 1955 and synthesized in 1960, is a deltahedral cluster whose stability is explained by Wade's rule. According to this rule, a *closo*-deltahedral cluster cage with n vertices requires $(n + 1)$ pairs of electrons that occupy $(n + 1)$ cluster bonding molecular orbitals.[3] This is the case for $[B_{12}H_{12}]^{2-}$, the *closo*-dodecaborate anion, which has 12 vertices and 13 pairs of electrons for cluster bonding. Modern synthetic methods have led to the synthesis of perhalogenated $[B_{12}X_{12}]^{2-}$ ions, where all twelve B–H bonds are replaced by B–X bonds. More than a decade ago, $[B_{12}X_{12}]^{2-}$ (X = F, Cl, Br) were synthesized[4–6] and are currently available in good yields under mild conditions. The substitution of all H ligands by halogens or pseudohalogens (*e.g.*, CN) leads to outstanding properties. For example, $[B_{12}(CN)_{12}]^{2-}$ exhibits the highest electronic stability of a dianion measured to date and was used to generate $[B_{12}(CN)_{11}]^-$, the first anion that binds to the noble gas argon at room temperature.[7] $H_2B_{12}Cl_{12}$ and $H_2B_{12}Br_{12}$ were the first solid diprotic superacids described.[8] In addition, $[B_{12}X_{12}]^{2-}$ anions (X = Br, Cl) have been used to keep highly reactive cations available in the condensed phase.[9]

Cleavage of an X ligand from $[B_{12}X_{12}]^{2-}$ can cause the uncoordinated boron atom to be electrophilic and reactive. Even though the doubly charged $[B_{12}X_{12}]^{2-}$ anions (X = F, Cl, Br, I) are exceptionally stable, the cleavage of X^- can be induced in the gas phase by collision-induced dissociation (CID) inside a mass spectrometer,[7,10] giving access to a "naked" boron atom in $[B_{12}X_{11}]^-$. The cleavage can be homolytic or heterolytic, depending on whether the ligand X is removed in its neutral or anionic form. Using CID, Warneke and collaborators have obtained new boron cluster ions that have never been synthesized before.[11,12] Additionally, they have found that fragmentation of these $[B_{12}X_{12}]^{2-}$ anions in the gas phase strongly depends on the identity of the X substituent. Under moderate excitation energies, they found that for X = I, the main fragmentation pathway for $[B_{12}I_{12}]^{2-}$ is a homolytic bond cleavage producing $[B_{12}I_{11}]^{2-\bullet}$. The heterolytic product $[B_{12}I_{11}]^-$ is also detected but in a lower quantity. Another abundant fragment detected was $[B_{12}I_{10}]^{2-}$ which results from a subsequent homolytic cleavage from $[B_{12}I_{11}]^{2-\bullet}$. $[B_{12}I_{10}]^{-\bullet}$ is also measured but has a lower abundance.

As we move towards smaller halogen substituents, the tendency towards homolytic cleavage decreases. For X = Br, the $[B_{12}Br_{11}]^-$ product is preferred over $[B_{12}Br_{11}]^{2-\bullet}$ although

[a] Department of Chemistry, Virginia Commonwealth University, Richmond, VA 23284, USA
[b] Department of Physics, Virginia Commonwealth University, Richmond, VA 23284, USA. E-mail: pjena@vcu.edu

both are detected. For the next cleavage, producing two unsubstituted boron atoms, the fragment $[B_{12}Br_{10}]^{-\bullet}$ is almost exclusively measured. For X = Cl, the $[B_{12}Cl_{11}]^-$ fragment is almost exclusively detected. Finally, for X = F, there is only electron detachment to produce $[B_{12}F_{12}]^{-\bullet}$.

At higher CID excitation energies, the B core is degraded with loss of BX or BX_3 fragments when X is F and Cl. When Br is the ligand, there is further $Br^\bullet$ loss up to having five naked boron atoms. Then, there is a competition between eliminating $Br^\bullet$ and BBr/BBr_3 fragments. When I is the substituent, the B_{12} unit does not degrade even after detaching all the ligands. However, Farràs *et al.* showed evidence of a transition from the dodecahedral shape structure to a planar structure.[13] They found that the icosahedral structure of a partly substituted dodecaborate is no longer stable when five or fewer iodine substituents are present. For six and seven substituents, temperature determines the relative stability, and energetically accessible isomers that were neither icosahedral nor planar were found. Overall, experimental evidence shows the possibility of having dodecahedral clusters with multiple unsubstituted boron atoms when the ligands are iodine and bromine.

The cleaved structures have interesting properties. One example of this is the discovery of superelectrophilic boron, even capable of binding to noble gases.[7,10,14] Kilic *et al.* computationally investigated the stability and catalytic potential of the $[B_{12}X_{11}]^{2-\bullet}$ dianions.[15] They found that species with X = F, Cl, Br, I, and CN are stable, especially $[B_{12}(CN)_{11}]^{2-\bullet}$ with a second electron binding energy of 3.17 eV. Stability increases due to ligand size and electron affinity. They demonstrated that these dianions can activate CO_2 and N_2, as indicated by the bond elongation in adsorbed CO_2/N_2 and a bent CO_2 geometry. Later, these authors expanded the scope of their study by including other small molecules like H_2, O_2, CO, and NH_3 and evaluated their interaction with $[B_{12}X_{11}]^{2-\bullet}$ and $[B_{12}X_{11}]^-$ for X = H, F, and CN.[16] Motivated by these studies, we explored the potential of these species to split water. Here, we present our results on hydrogen production by $[B_{12}X_{10}]^{-\bullet}$ type clusters (with X = Br, I).

2 Computational methods

All calculations of neutral and ionic species were conducted using density functional theory (DFT) as implemented in Gaussian 16 software,[17] employing the restricted Kohn–Sham formalism for closed-shell species and the unrestricted formalism for open-shell species. Geometry optimizations and the corresponding frequency calculations were done to verify the presence of true minima. Optimizations used the default convergence thresholds. We employed the B3LYP hybrid functional[18,19] in combination with the Stuttgart/Dresden effective core potential (SDD ECP) for iodine[20] and the 6-31+G(d,p) basis set for the rest of the atoms,[21,22] as this approach previously performed in good agreement with experiment.[15] We performed additional tests using the aug-cc-pVTZ basis set[23] with and without D3(BJ) dispersion,[24] but the results were qualitatively the same in terms of energetics (see Section S1 of the SI for further details). Therefore, we continued our investigations using the previously mentioned level of theory.

The search for transition states (TSs) used the QST3 method, which combines quadratic synchronous transit interpolation with quasi-Newton optimization.[25] Another strategy was to perform a relaxed scan of a carefully selected degree of freedom to select a candidate geometry. A third strategy was the use of the nudged-elastic-band method,[26] as implemented in Orca 6.0,[27] in combination with the PBEh3c composite method developed by the Grimme group.[28] These three strategies generated a guess for the transition state, which was subsequently optimized using the level of theory described in the previous paragraph. Frequency calculations of the transition states found were then performed to verify that they only possessed a single imaginary frequency. This guaranteed the finding of a first-order saddle point on the potential energy surface (PES). A visual inspection of each imaginary frequency was performed to verify the correspondence with the expected reaction coordinate. Finally, the calculation of Hirshfeld charges, the conceptual DFT analysis, and the topological analysis of the electron localization function (ELF) were performed using Multiwfn version 3.8.[29]

3 Results and discussion

The relative energies of different $[B_{12}X_n]^q$ species (n = 11, 10; q = 2−, 1−, 0), as well as a quantitative measurement of their deviation from the perfect icosahedral geometry, and the charge distribution between the cluster core and the ligands are discussed in Section 3.1. This section also discusses the electron-accepting capabilities of the different atomic sites within these species, particularly those of the unsubstituted boron atoms, using the condensed Fukui function, a concept derived from conceptual DFT. Section 3.2 discusses the different homolytic and heterolytic pathways leading to dodecaborate clusters with one or two uncoordinated boron atoms starting from $[B_{12}X_{12}]^{2-}$ clusters (X = Br, I, CN). We used DFT to calculate the relative energies for ligand-detachment pathways. Knowledge of the preferred path for ligand removal is important for understanding the reactivity of dodecaborate ions and their derivatives. Section 3.3 discusses the thermodynamics of the reactions of dodecaborate clusters with one and two unsubstituted boron atoms with water. And finally, Section 3.4 discusses the mechanisms of H_2 production from clusters of the $[B_{12}X_{10}]^{-\bullet}$ type (X = Br, I), as well as subsequent reactions.

3.1 Energetics, charge distribution, and electron-accepting behavior in clusters of the $[B_{12}X_n]^q$ type

Table 1 lists the relative energies of the $[B_{12}X_n]^q$ species (q = 2−, 1−, 0) with respect to $[B_{12}X_n]^{2-}$ for a given value of n (11 or 10), including zero-point energy (ZPE). It can be observed that within the series for each particular substituent, the lower energy corresponds to $[B_{12}X_n]^{2-}$, followed by $[B_{12}X_n]^-$, and

Table 1 Relative energy including zero-point energy (eV), RMSD with respect to $[B_{12}X_{12}]^{2-}$ (Å), core total charge (CTC), and substituent total charge (STC) in units of *e* (elementary charge) for different $[B_{12}X_n]^q$ species (n = 11, 10; q = 2−, 1−, 0) with naked boron atoms

	X = Br			X = I			X = CN		
Species	E	RMSD	CTC (STC)	E	RMSD	CTC (STC)	E	RMSD	CTC (STC)
$[B_{12}X_{11}]^{2-\bullet}$	0.00	0.02	−0.25 (−1.75)	0.00	0.03	−0.52 (−1.48)	0.00	0.01	0.27 (−2.26)
$[B_{12}X_{11}]^{-}$	1.29	0.07	−0.01 (−0.99)	1.47	0.07	−0.36 (−0.64)	3.14	0.08	0.68 (−1.67)
$[B_{12}X_{11}]^{\bullet}$	6.99	0.08	0.08 (−0.08)	6.70	0.07	−0.40 (0.40)	11.50	0.08	0.85 (−0.85)
$[B_{12}X_{10}]^{2-}$	0.00	0.07	−0.24 (−1.76)	0.00	0.07	−0.45 (−1.55)	0.00	0.06	0.18 (−2.18)
$[B_{12}X_{10}]^{-\bullet}$	1.27	0.07	0.01 (−1.01)	1.43	0.07	−0.31 (−0.69)	2.75	0.07	0.63 (−1.63)
$B_{12}X_{10}$	6.73	0.09	0.22 (−0.22)	6.60	0.09	−0.20 (0.20)	10.28	0.09	1.01 (−1.00)

$[B_{12}X_n]$; irrespective of having one or two unsubtituted boron atoms (n = 11 or 10, respectively). It is also noteworthy that the relative energies when the substituents are bromine and iodine are somewhat similar within each series, but when CN is the ligand, those energy differences increase to a large extent, accounting for the ''extreme'' electronegativity of the CN fragment.

Also listed in Table 1 is the root-mean-square distance (RMSD) of the boron core of each species with respect to the boron core of the corresponding $[B_{12}X_{12}]^{2-}$ species. These last species are considered the point of comparison because they basically correspond to perfect icosahedra. The purpose of calculating the RMSD is to quantify how much a given species deviates from the corresponding perfect icosahedron. Generally speaking, none of the species deviates much from ideality since the RMSD ranges from 0.01 to 0.09 Å. We can also observe that the $[B_{12}X_n]^{2-}$ species deviates the least from the perfect icosahedron within each particular series, but the deviation is considerably smaller for the $[B_{12}X_{11}]^{2-\bullet}$ species.

Finally, the last quantities in Table 1 correspond to the sum of the Hirshfeld charges on the core of the dodecaborate cluster (core total charge, CTC) and the sum of the charges on the cluster's substituents (substituent total charge, STC). The reason for calculating these quantities was to evaluate the influence of the different charge states and ligands on the charge distribution between the core and ligands. For the charged species of $[B_{12}Br_n]^q$ type, it can be observed that the negative charge basically resides on the substituents, while this is no longer true for the charged species $[B_{12}I_n]^q$, where there is an increment of the negative charge residing on the core of the cluster. This can be explained in terms of the higher electronegativity of bromine compared to iodine. The effect of electronegativity is more pronounced in the case of CN, as evidenced by the fact that the cluster core is positively charged to counteract the large negative charge distributed among the ligands.

Fukui function is an important concept in conceptual density functional theory (CDFT). It indicates the change in electron density at a given molecular site when the number of electrons is changed.[30,31] Under its finite difference version, it takes the form shown in eqn (1) for the addition of an electron (nucleophilic attack):

$$f^{+}(r) = \rho_{N+1}(r) - \rho_N(r) \quad (1)$$

$$f_i^{+} = q_N^i - q_{N+1}^i \quad (2)$$

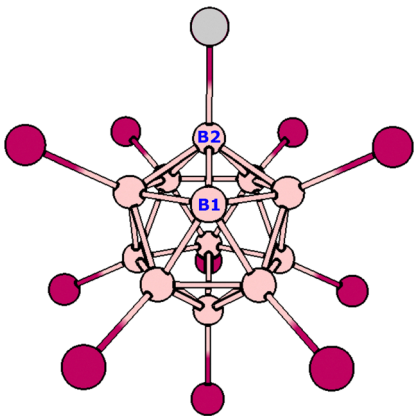

Fig. 1 Dodecaborate cluster with one unsubstituted boron atom labeled B1. The potential removal of an additional substituent, marked in gray color, would leave a second unsubstituted boron atom labeled B2.

where ρ_{N+1} and ρ_N corresponds to the electron density of the system with $N + 1$ electrons and N electrons, respectively. This definition can yield a qualitative yet useful description of the electronic structure. However, if we want to use the Fukui function quantitatively, we should consider the so-called condensed Fukui function, which is shown in eqn (2).[32] Here, i denotes a particular nucleus and q denotes charge. There are multiple ways to calculate atomic charges, though there is no consensus on which method is ideal for calculating the condensed Fukui function. However, the Hirshfeld charge scheme has proven to be a very suitable choice.[33] Using this approach, we intend to quantify the propensity of the unsubstituted boron atoms in these species to accept an electron. This should be related to their susceptibility to nucleophilic attack or, in other words, to their Lewis acidic character.

Fig. 1 shows a dodecaborate cluster with one unsubstituted boron atom labeled B1; it also shows one of the substituents in grey, indicating that if that substituent is removed, the cluster will be left with a new naked boron atom labeled B2.

Fig. 2 shows the different values of the condensed Fukui function: on the unsubstituted boron atoms (pink bars), the sum over the entire boron core, including the uncoordinated boron atom(s) (cyan), and the sum over the substituents (blue) for all the species considered in this section. It is worth noting that the pink bars in panels a, b, and c represent only one boron atom (B1), while in panels d, e, and f they represent the sum of two boron atoms (B1 and B2). It is also important to mention

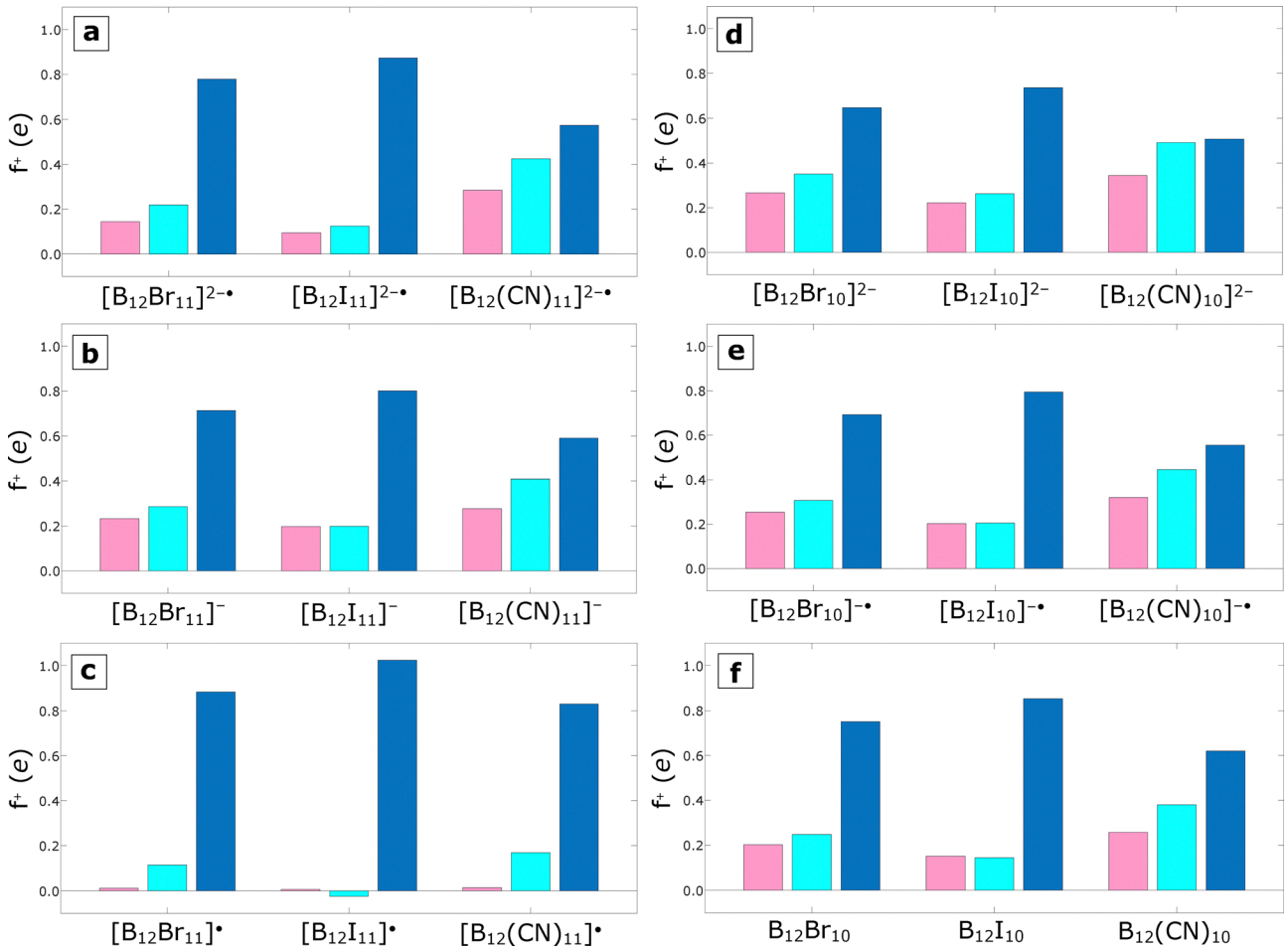

Fig. 2 Condensed Fukui functions on the unsubstituted boron atom(s) (pink), over the entire boron core (cyan), and over the substituents (blue). The corresponding species are noted at the bottom of each panel. The pink bars in panels a, b, and c represent only one boron atom (B1), while in panels d, e, and f they represent the sum of over two boron atoms (B1 and B2, see Fig. 1).

that the sum of the condensed Fukui function over all atoms within a particular molecule equals one. In simple terms, the condensed Fukui function is one spread over the whole molecule, with the particular distribution depending on each atom's capability for accepting electrons. For the systems shown in Fig. 2, the comparison between the pink bars and the cyan bars tells us that the Fukui function, and therefore the electron-accepting capability, of the core is mainly located in the unsubstituted boron atoms, as the size of the bars is comparable for all them, except for systems of the $[B_{12}X_{11}]^{\bullet}$ type (Fig. 2c) in which the electron-accepting character remains mainly in the substituted boron atoms. Another general trend we observe is the influence of the substituent on the Fukui function of the unsubstituted boron atom(s) and, therefore, on their electron-accepting capability. The panels in Fig. 2 show that the pink bar in each series is largest when the substituent is CN, followed by Br, and then by I. This observation correlates with the well-known electronegativity order of the substituents (CN > Br > I). This fact, along with the nature of the Fukui function, results in the CN-containing species having the smallest condensed Fukui function sum over the substituents (blue bars in Fig. 2). All optimized geometries, Hirshfeld charges, and condensed Fukui function values related to this section, and summarized in Table 1 and Fig. 2, can be found in Section S2 of the SI.

3.2 Homolytic/heterolytic dissociations from $[B_{12}X_{12}]^{2-}$

As mentioned previously, the fragmentation reactions of $[B_{12}X_{12}]^{2-}$ species strongly depend on the identity of the X substituent. In this section, we discuss the thermodynamics of these fragmentation reactions and provide insights into relevant kinetic aspects. Since we are interested in describing the reactivity of dodecaborate-based clusters having one or two unsubstituted boron atoms, we restrict our analysis to the different fragmentation pathways starting from $[B_{12}X_{12}]^{2-}$ species and leading to species of the type $[B_{12}X_{10}]^{q}$ (X = Br, I, CN; $q = 2-, 1-, 0$). Fig. 3 summarizes such possible pathways. Here, we emphasize the heterolytic or homolytic nature of the bond cleavage and which kind of fragmentation leads to the thermodynamic or the kinetic products (respectively marked as "*t*" or "*k*" within parentheses). The computational results that give

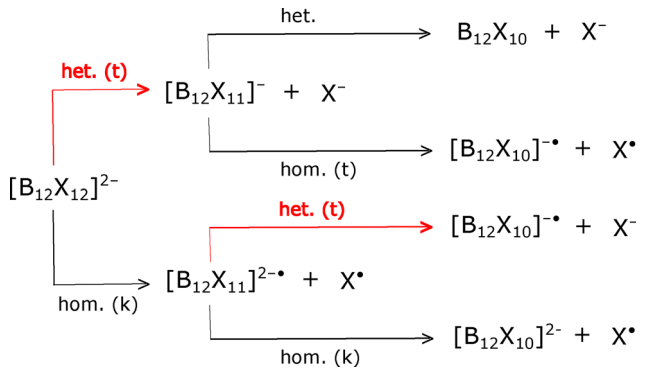

Fig. 3 Summary of the homolytic (hom.) and heterolytic (het.) pathways going from $[B_{12}X_{12}]^{2-}$ to $[B_{12}X_{10}]^q$ species (X = Br, I, CN; q = 2−, 1−, 0). Labels "*t*" and "*k*" correspond to thermodynamic and kinetic products. Red arrows mark fragmentations with a Coulomb barrier.

Table 2 Gibbs free energy changes (in eV) at 298.15 K for homolytic (hom.) and heterolytic (het.) bond cleavages starting from different $[B_{12}X_n]^q$ initial species (n = 12, 11; q = 2−, 1−). The numbers within parentheses are the Gibbs free energies of the corresponding transition states relative to the initial species in eV

Initial species	X = Br		X = I		X = CN	
	hom.	het.	hom.	het.	hom.	het.
$[B_{12}X_{12}]^{2-}$	4.51	2.24 (3.34)	3.04	1.14 (2.32)	6.21	4.46 (5.49)
$[B_{12}X_{11}]^-$	3.97	5.83	2.58	4.35	5.45	8.07
$[B_{12}X_{11}]^{2-\bullet}$	4.02	1.69 (2.63)	2.64	0.68 (1.76)	5.86	3.69 (4.51)

rise to this distinction are presented in Table 2 and will be further discussed in the rest of this section.

Table 2 shows the Gibbs free energy changes at 298.15 K associated with different homolytic and heterolytic bond dissociation reactions starting from $[B_{12}X_{12}]^{2-}$, $[B_{12}X_{11}]^-$, and $[B_{12}X_{11}]^{2-\bullet}$ species. These species are indicated in Fig. 3. From the values in Table 2, we can see that the heterolytic fragmentations of $[B_{12}X_{12}]^{2-}$ are thermodynamically more favorable than the homolytic ones for all the ligands considered in this work. However, as discussed previously, Warneke *et al.* found different amounts of the homolytic products depending on the identity of the substituent,[11,12,34] with significant amounts of the homolytic products for bromine and particularly for iodine. A rationalization of these experimental observations can be based on the existence of high-energy transition states for the heterolytic fragmentations. In other words, the heterolytic and thermodynamically favored cleavage could be kinetically controlled or suppressed. The origin of this kinetic control has previously been explained in terms of a repulsive Coulomb barrier arising from the formation of two negatively charged fragmentation products.[35] To further explore this, we proceed to find the hypothesized transition state. Our strategy was to perform a scan of one of the B-X bonds in $[B_{12}X_{12}]^{2-}$, relaxing the remaining degrees of freedom at each step, *i.e.*, a relaxed scan. It is important to mention that the multiplicity of the system as a whole was kept as a singlet, even for long B–X distances. We quantified the natural charges during the scan and confirmed that the X fragment retained a negative charge, consistent with heterolytic cleavage. Details of the relaxed scans and the natural charges can be found in Section S3 of the SI. The geometry corresponding to the energy maximum within the scan was used as a starting point for transition-state optimization, along with a frequency calculation to confirm the presence of a first-order saddle point. Using this methodology, we were able to determine the transition states involved in the heterolytic cleavage of $[B_{12}X_{12}]^{2-}$ (X = Br, I, CN), whose energies are listed within parentheses in Table 2. The B–X distances for these transition states were 6.02, 5.30, and 6.06 Å for Br, I, and CN, respectively. The geometries and frequencies of these transition states are presented in Section S3 of the SI.

At this point, it is instructive to compare the computational results of Farràs *et al.* on the dissociation of $[B_{12}I_{12}]^{2-}$ with the results obtained in this work.[13] These authors found the heterolytic cleavage to be favored over the homolytic one by 1.55 eV, compared to 1.9 eV in this work. The discrepancy can be attributed to the different levels of theory used in both works: Farràs and collaborators optimized geometries using the BP86 functional,[36,37] considered scalar relativistic corrections using the zero-order regular approximation (ZORA) formalism,[38] and used an all-electron basis of triple-zeta plus polarization quality (not completely specified but referred to as TZP). Their geometry optimization was followed by single-point calculations at the B3LYP/ZORA/TZP level of theory. In this work, as described previously, we optimized geometries using the B3LYP functional in combination with the SDD ECP for iodine and the 6-31+G(d,p) basis set for the boron atoms and considered the energy of the optimized structure at the same level of theory. It is worth noting that the SDD ECP includes scalar-relativistic effects *via* parameterization derived from relativistic atomic calculations, while ZORA explicitly incorporates relativity through a modified kinetic energy operator in the Hamiltonian. Additionally, all the thermodynamic discussion in this work is given in terms of the Gibbs free energy at 298.15 K, *i.e.*, considering thermal and entropic contributions on top of the energetic one at 0 K, while the discussion by Farràs seems to be done only in terms of the energetic contribution at 0 K. Despite the mismatch, both approaches predict the heterolytic cleavage to be more favorable. Regarding the transition state, Farràs *et al.* attempted to model the transition state involved in the fragmentation to $[B_{12}I_{11}]^-$ and I^- starting from the singlet electronic state of the parent $[B_{12}I_{12}]^{2-}$ cluster using second-order Møller–Plesset perturbation theory single-point calculations on Hartree–Fock optimized geometries employing 6-311+G(d) and 6-311G(d) basis sets for boron and iodine, respectively. Using this approach, they found a transition state with an energy of 3.98 eV and a B–I distance of 5.40–6.00 Å. Using our methodology, we found a transition state with a Gibbs free energy of 2.32 eV and a B–I distance of 5.30 Å. The difference in the energy might be analogously explained by the very different approaches employed, but in either case, both works point to transition states with very elongated B–I bonds. As far as we know, no CID experiments have been performed to study $[B_{12}(CN)_{12}]^{2-}$ fragmentation, but based on our computed results shown in Table 2, we can expect an analogous behavior to

the cases when the ligands are Br and I with both the heterolytic and homolytic products present.

For the dissociation from $[B_{12}X_{11}]^-$, Fig. 3 shows that both possible fragmentation pathways produce only one charged product; therefore, the presence of the so-called Coulomb barrier is not expected for any of them and we can simply state that the thermodynamic homolytic product is the one favored for the three substituents (see Table 2). The case of $[B_{12}X_{11}]^{2-\bullet}$ is different since the heterolytic cleavage can produce two charged fragments, and, therefore, a Coulomb barrier is expected. The fragmentation of $[B_{12}X_{11}]^{2-\bullet}$ is analogous to the one for $[B_{12}X_{12}]^{2-}$ in the sense that even when the heterolytic dissociation is thermodynamically favored, this is kinetically controlled and both products can be expected although in different proportions depending on the identity of the ligand. The Gibbs free energies of the corresponding transition states are shown within parentheses in Table 2. These previous arguments justify further study of the reactivity of vacant boron sites within species of the kind $[B_{12}X_n]^q$ (n = 11, 10; q = 2−, 1−) (see Fig. 3).

3.3 Reactions of $[B_{12}X_n]^q$ (n = 11, 10; q = 2−, 1−) with water

Warneke and collaborators gathered evidence through CID experiments that vacant boron atoms within $[B_{12}I_n]^-$ species with n = 11 to 8 readily added water molecules, ultimately recovering a structure with twelve ligands.[11,12] Eqn (3) describes the reaction of clusters of the $[B_{12}X_{11}]^q$ type (q = 2−, 1−) with one water molecule. For this and the rest of the reactions considered in this work, the Gibbs free energy change was calculated by subtracting the Gibbs energy of the reactants from the Gibbs energy of the products. The corresponding energy changes when the substituents are Br, I, and CN are shown in Table 3. We can observe that when q = 2−, all the reactions are endergonic; however, the energy required is not very high and corresponds to 0.5, 0.2, and 0.9 eV for Br, I, and CN, respectively. Alternatively, when q = 1−, all reactions are exergonic and therefore spontaneous, in line with Warneke's experimental findings.

$$[B_{12}X_{11}]^q + H_2O^- \rightarrow [B_{12}X_{11}(H_2O)]^q \quad (3)$$

$$[B_{12}X_{11}(H_2O)]^{q-} \rightarrow [B_{12}X_{11}(OH)]^q + H^\bullet \quad (4)$$

$$[B_{12}X_{11}(OH)]^{q-} \rightarrow [B_{12}X_{11}]^q + OH^\bullet \quad (5)$$

Equation 4 represents the generation of a hydrogen atom from the $[B_{12}X_{11}(H_2O)]^q$ species generated after a water molecule is attached to the uncoordinated boron atom. Table 3 shows that when q = 2−, this reaction is exergonic when the ligands are Br and CN and slightly endergonic when the substituent is I. Alternatively, when q = 1−, the reaction is highly endergonic for the three ligands. Finally, eqn (5) describes the process in which $OH^\bullet$ detaches from the boron cluster, leaving a vacant boron atom. This step is important if we want to reuse the catalytic site to perform the reactions described in eqn (3) and (4), resulting in $H^\bullet$ production. Unfortunately, the $OH^\bullet$ detachment process is highly endergonic for both the cases with q = 2− and q = 1−. Summarizing, species of the kind $[B_{12}X_{11}]^{2-}$ (X = Br, I, and CN) could have some interest for $H^\bullet$ production since they require little energy to attach a water molecule to the uncoordinated boron atom and then release $H^\bullet$ either spontaneously (X= Br and CN) or with a small energy input (X = I). However, the $OH^\bullet$ detachment step required for catalyst recycling is energetically forbidden for all the ligands.

Eqn (6) and (7) describe the consecutive reactions of $[B_{12}X_{10}]^q$ (X = Br, I, CN; q = 2−, 1−) species with water in order to get a substituent on each of the twelve boron atoms. The corresponding Gibbs free energy changes are given in Table 4. We were not able to find stable products of the form $[B_{12}X_{10}(H_2O)_2]^{2-}$ for any of the ligands. Additionally, the $[B_{12}(CN)_{10}(H_2O)_2]^-$ product could not be found. This leaves us with only two possible species incorporating two water molecules: $[B_{12}Br_{10}(H_2O)_2]^{-\bullet}$ and $[B_{12}I_{10}(H_2O)_2]^{-\bullet}$. In the following section, we will study some of the reaction pathways starting from these two species.

$$[B_{12}X_{10}]^q + H_2O^- \rightarrow [B_{12}X_{10}(H_2O)]^q \quad (6)$$

$$[B_{12}X_{10}(H_2O)]^q + H_2O^- \rightarrow [B_{12}X_{10}(H_2O)_2]^q \quad (7)$$

3.4 Mechanisms of H_2 production

As mentioned in Section 3.3, there are two dodecaborate-based clusters capable of attaching two water molecules among the species studied in this work. These species are $[B_{12}Br_{10}]^{-\bullet}$ and $[B_{12}I_{10}]^{-\bullet}$. The importance of the attachment of these two water molecules lies in the possibility that it could lead to the production of molecular hydrogen. In this section, we explore some mechanistic aspects of H_2 production after the incorporation of two water molecules on the naked boron atoms within the previously mentioned moieties.

Fig. 4 details two possible reaction mechanisms starting from $[B_{12}Br_{10}(H_2O)_2]^{-\bullet}$, labeled as species I. Both mechanisms go through transition state TS1 to produce.

$[B_{12}Br_{10}(OH)_2]^{-\bullet}$ (intermediate II) and H_2. TS1 has a relative Gibbs free energy of 0.06 eV with respect to I, indicating that the first step in H_2 production is basically barrierless. Starting

Table 3 Gibbs free energy changes (in eV) at 298.15 K for reactions described in eqn (3) and (4) starting from species with q = 2− and q = 1−

	X = Br			X = I			X = CN		
Charge	Eqn (3)	Eqn (4)	Eqn (5)	Eqn (3)	Eqn (4)	Eqn (5)	Eqn (3)	Eqn (4)	Eqn (5)
q = 2−	0.5	−0.4	4.9	0.2	0.1	4.7	0.9	−0.8	5.0
q = 1−	−1.8	3.0	3.8	−1.6	2.7	3.9	−2.0	3.6	3.5

Table 4 Gibbs free energy changes (in eV) at 298.15 K for the reactions described in eqn (6) and (7) starting from species with $q = 2-$ and $q = 1-$

	X = Br		X = I		X = CN	
Charge	Eqn (6)	Eqn (7)	Eqn (6)	Eqn (7)	Eqn (6)	Eqn (7)
$q = 2-$	0.10	—	0.02	—	−4.02	—
$q = 1-$	−1.25	0.49	−1.16	0.22	−1.44	—

from intermediate II, we propose two possible reaction pathways. The first involves two consecutive barrierless $OH^{\bullet}$ detachments to give intermediate VI and the final product V, *i.e.*, the dodecaborate cluster with two unsubstituted boron atoms. The barrierless character of these bond-breaking events was confirmed through relaxed scans, both of which increase monotonically in energy without showing a maximum that could be associated with a transition state. The other pathway involves the production of a second H_2 molecule to generate intermediate III. At this point, it is worth mentioning that there should be a competition between reaching intermediate VI and TS2, since the corresponding relative energies are 1.58 and 1.73 eV, respectively. Therefore, under experimental conditions, which normally involve a distribution of energies, there should be a branching between the two pathways. Additionally, it should be noted that there is a very high energetic cost of 4.27 eV for going from species VI to V, and this might contribute to having a fraction of $[B_{12}Br_{10}OH]^-$ as the final product. On the other hand, the transformation between intermediate III and IV, occurring through TS3, involves a change in the O–O distance, from 3.30 to 1.46 Å (closer to the O_2 molecular bond length of 1.21 Å) and an energetic barrier of 2.21 eV. Actually, the oxygen atoms within species IV form a four-membered ring with two boron atoms (see Fig. 4). Finally, molecular oxygen is produced during the transition from species IV to V through TS4 with an energetic barrier of 2.70 eV. The absolute and relative Gibbs free energies and geometries of the species shown in Fig. 4 and 5 are given in Section S4 of the SI. Additionally, the vibrational frequencies for the transition states, which show only one imaginary frequency, are given in the same section.

Fig. 5 shows two reaction pathways for $[B_{12}I_{10}(H_2O)_2]^{-\bullet}$ (species VII). As in the case when iodine is the ligand, both pathways start with the generation of H_2 upon reaching TS5. It is important to note that the Gibbs free energy corresponding to TS5 appears as negative. This behavior arises because minima and transition states are localized on the Born–Oppenheimer surface, and other contributions, such as the thermal (which includes the zero-point energy) and entropic ones, are added on top of that.[39–41] In this particular case, if we only consider the Born–Oppenheimer energy relative to VII, we have

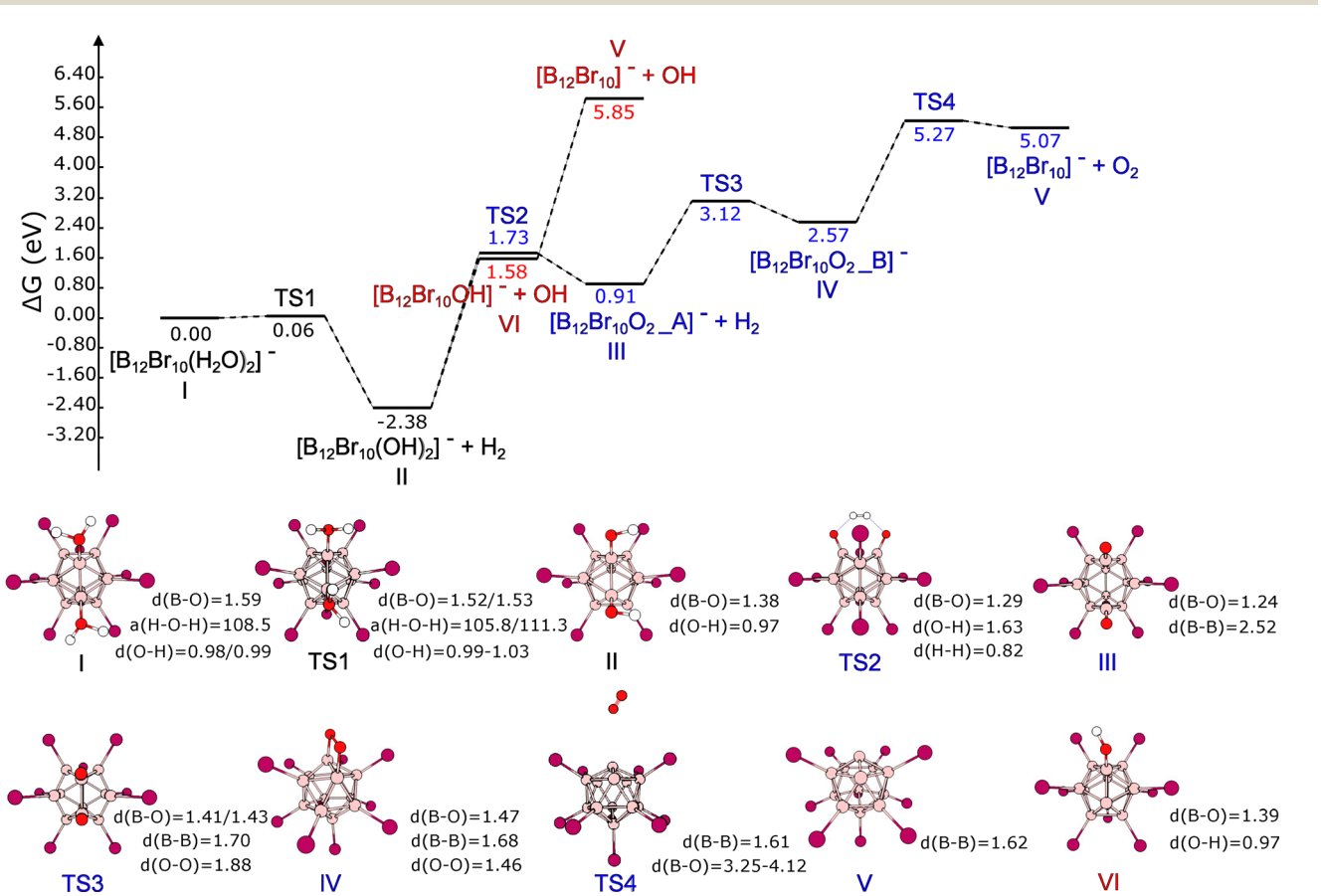

Fig. 4 Relative Gibbs free energy diagram (in eV) at 298.15 K for H_2 production starting from $[B_{12}Br_{10}(H_2O)_2]^{-\bullet}$ and subsequent reactions. The bottom of the figure shows the geometries of all species involved with distances in Å (denoted as "d") and angles in degrees (denoted as "a") important in bond-breaking and bond-forming processes.

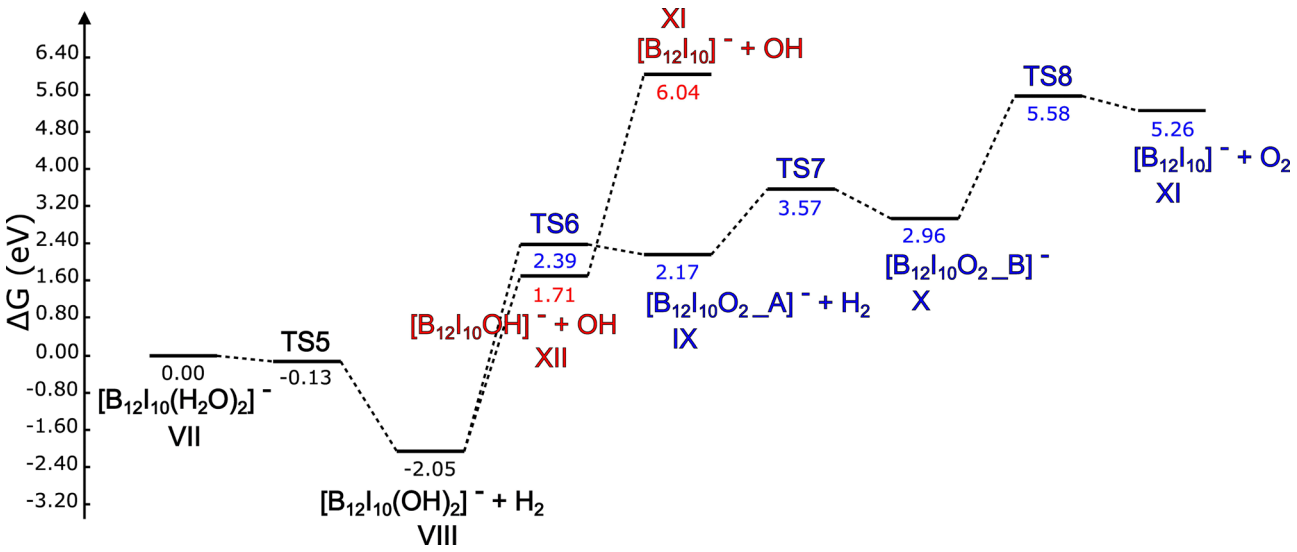

Fig. 5 Relative Gibbs free energy diagram (in eV) at 298.15 K for H_2 production starting from $[B_{12}I_{10}(H_2O)_2]^{-\bullet}$ and subsequent reactions.

0.09 eV for TS5 and −1.44 eV for products VIII plus H_2. Under these conditions, TS5 effectively looks like a barrier. After adding the above-mentioned contributions or corrections, this H_2 production reaction can be regarded as barrierless. This point underscores the importance of considering both thermal and entropic contributions when discussing reaction mechanisms.

After producing intermediate VIII and H_2, we again observe two consecutive $OH^{\bullet}$ barrierless detachments, confirmed by relaxed scans as discussed previously. We also have a high energetic cost of 4.33 eV to go from intermediate XII to XI, giving rise to the possibility of having the $[B_{12}I_{10}OH]^-$ product. Additionally, TS6 is 0.68 eV above product XII plus $OH^{\bullet}$. Therefore, it is reasonable to expect that a good fraction of intermediate VIII will go into producing XII rather than producing IX and a second H_2 molecule. For the fraction of VIII that converts into IX, the rest of the pathway is analogous to the one shown in Fig. 4, with TS7 leading to the formation of a four-membered ring involving two oxygen and two boron atoms within X. Finally, TS8 precedes the formation of molecular oxygen and XI, the original cluster with two unsubstituted boron atoms.

Finally, in order to get more insights into the way a specific modification of the dodecaborate ion facilitates the O-H bond cleavage during hydrogen generation, we performed a topological analysis of the electron localization function (ELF).[42,43] In this context, each local maximum of this function is called an attractor, and can be classified into the core, bonding, and non-bonding categories. We performed this analysis for $[B_{12}Br_{10}(H_2O)_2]^{-\bullet}$ and $[B_{12}I_{10}(H_2O)_2]^{-\bullet}$ (species I and VII on Fig. 4 and 5 respectively), but since we are interested in the cleavage of the water moieties within these species, and for the sake of clarity in the discussion, Fig. 6 only shows the fragments of species I and VII near the water molecules. In Fig. 6a, we can see such a fragment for $[B_{12}Br_{10}(H_2O)_2]^{-\bullet}$ as well as the attractors (shown as green spheres and labeled as in the Multiwfn output) related to the water moieties. The water molecule linked to boron atom 1 (B1) in Fig. 6a is shown in transparent form to facilitate visualization of the corresponding attractors. At this point, we want to briefly describe some situations regarding these attractors: bonding attractor 95 lies between the core attractors for boron (not shown) and oxygen. Non-bonding attractor 69 corresponds to an oxygen lone pair. Attractor 102, corresponding to the oxygen core, has coordinates very close to those of the oxygen nucleus, as is common for core attractors. Finally, although attractors 75 and 80 are very close to the hydrogen nuclei, they should be identified as O–H bonding attractors because hydrogen does

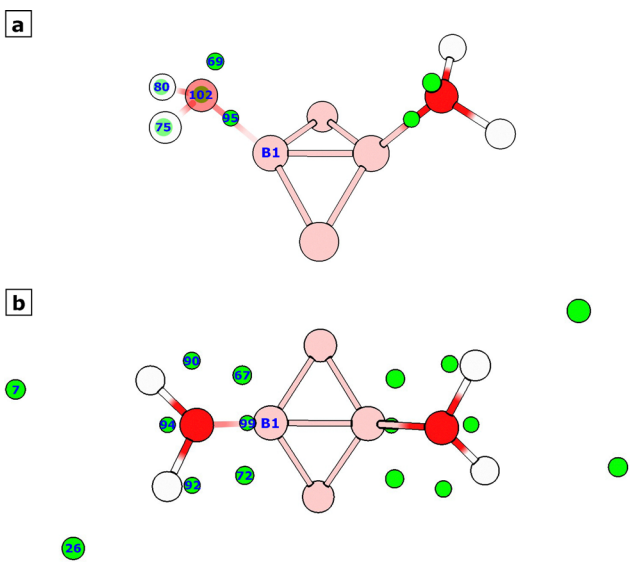

Fig. 6 Fragments surrounding the water moieties within (a) $[B_{12}Br_{10}(H_2O)_2]^{-\bullet}$ and (b) $[B_{12}I_{10}(H_2O)_2]^{-\bullet}$. The ELF attractors related to the water moieties are shown as green spheres. On panel (a), a water molecule and its bond to the B1 atom are shown transparently to allow visualization of the corresponding attractors. In panel (b), only the B1–O bond is shown in transparent form for the same reason.

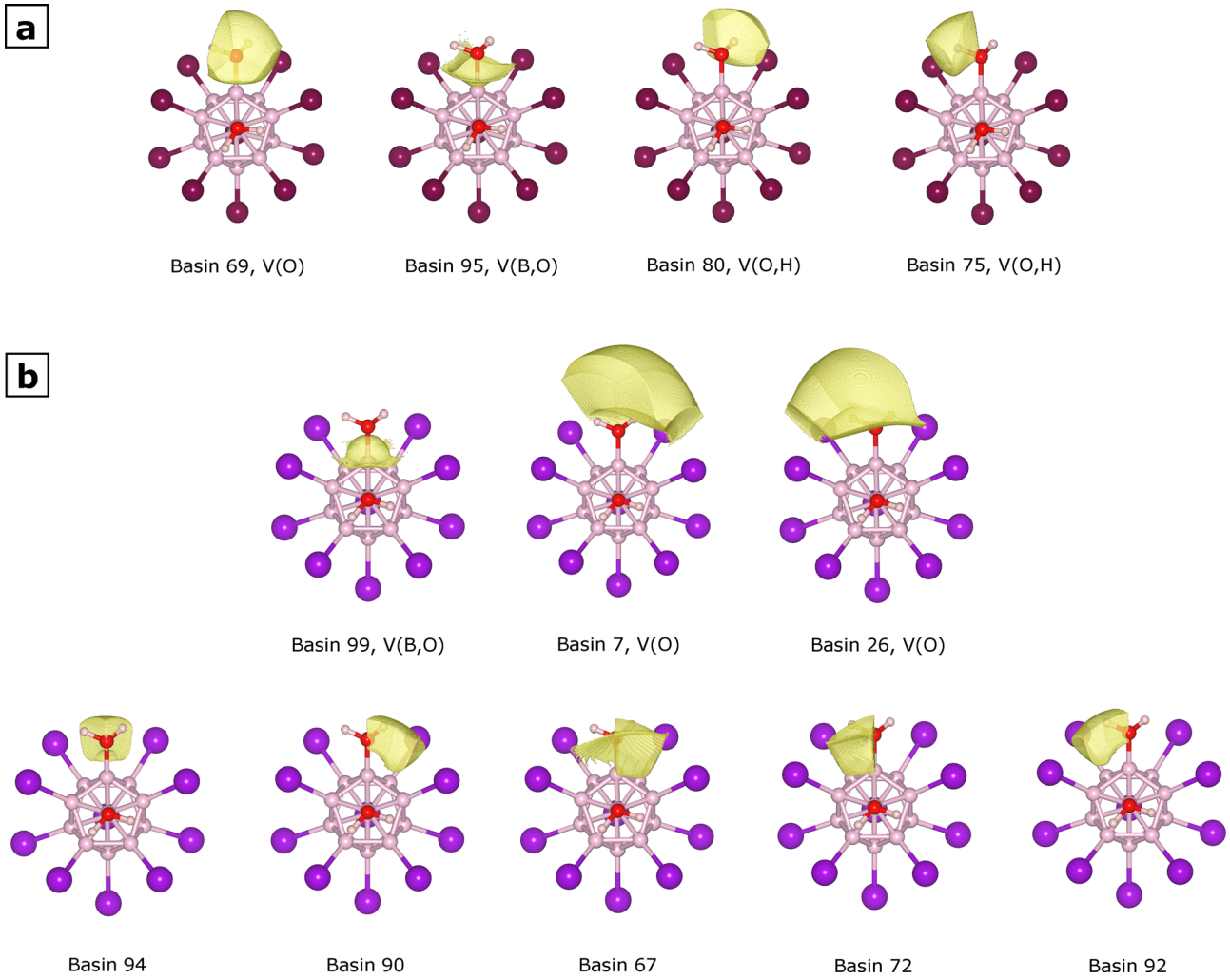

Fig. 7 ELF basins related to the water moiety bonded to the boron atom labeled as B1 in Fig. 6 within (a) $[B_{12}Br_{10}(H_2O)_2]^{-\bullet}$ and (b) $[B_{12}I_{10}(H_2O)_2]^{-\bullet}$. The basins shown correspond to regions with electron density greater than 0.001 a.u.

not have core electrons, and these attractors contribute to the O–H bond. Each of these attractors is associated with a corresponding basin, and these can be visualized in Fig. 7a, with the exception of the oxygen core basin C(O), which has a very small volume and has an attractor that lies very close to the oxygen nucleus. Different basin properties can be estimated; in this work, we computed the average electron population (by integrating the electron density over each basin) and the volume. Table 5 lists those values for the basins associated with the attractors shown in Fig. 6a, as well as the corresponding labels describing the type of basin. We have an average electron population of 2.14 for the oxygen core –C(O)–, 2.46 for the oxygen lone pair –V(O)–, 1.79 for the B–O bond –V(B,O)–, and 1.83 for each of the O–H bonds –V(O,H). Therefore, the total electron population for this water moiety is 10.04. The situation is completely analogous when we consider the water molecule bonded to the other boron atom in Fig. 6a. For comparison, the total electron population of an isolated water molecule should roughly correspond to 10: two each for the oxygen core, the oxygen lone pairs, and the O–H bonds. Therefore, loosely speaking, each water moiety in $[B_{12}Br_{10}(H_2O)_2]^{-\bullet}$ can be regarded as forming some sort of dative bond with one boron atom through one of its lone pairs.

Table 5 Average electron population (in *e*), volume (in Å^3), and label for the basins corresponding to the ELF attractors found for $[B_{12}Br_{10}(H_2O)_2]^{-\bullet}$ and shown in Fig. 6a

Basin	Population	Volume	Label
102	2.14	0.04	C(O)
69	2.46	61.43	V(O)
95	1.79	2.07	V(B,O)
80	1.83	48.09	V(O,H)
75	1.83	74.99	V(O,H)

When we considered the water moieties in $[B_{12}I_{10}(H_2O)_2]^{-\bullet}$ described in Fig. 6b, 7 and Table 6, we could observe the following situations in comparison with the bromine substituted species I: basin 99 corresponds to the bonding type and pertains to the B–O bond, it has an electron population of 2.11. This is analogous to the V(B,O) basin found for species I. The fact that basins 7 and 26 have very large volumes compared to

Table 6 Average electron population (in *e*), volume (in Å^3), and label for the basins corresponding to the ELF attractors found for $[B_{12}I_{10}(H_2O)_2]^{-\bullet}$ and shown in Fig. 6b

Basin	Population	Volume	Label
99	2.11	1.87	V(B,O)
7	1.77	290.92	V(O)
26	1.09	217.79	V(O)
94	1.16	3.66	—
90	1.25	4.52	—
67	1.03	5.75	—
72	0.92	4.01	—
92	1.30	4.60	—

the other basins supports their classification as non-bonding basins (Table 6), as is well known for this basin type.[44] Visual inspection of these basins in Fig. 7b also points in the same direction. The corresponding populations are 1.77 and 1.09, respectively. This is in sharp contrast to species I, which had one non-bonding basin with an electron population of ~2. At this point, identifying the remaining basins for the water moiety in $[B_{12}I_{10}(H_2O)_2]^{-\bullet}$ becomes more difficult, as they depart significantly from the commonly observed patterns. However, we will offer some insights. The sum of the electron populations identified so far (basins 99, 7, and 26) is 4.98, while the total population for all the basins is 10.64 (Table 6). This means the population for the yet-to-be-identified basins is 5.66. If our current designations are correct, we still need to account for the oxygen core basin and the O–H bonding basins, which can naively be assumed to have a population of ~2 each to give a total of ~6, which reasonably matches the population of the unidentified basins. This means that those ~6 electrons should be distributed among the five unidentified basins, a very unexpected pattern. Additionally, the attractor for the oxygen core is no longer near the nuclear coordinates as was the case for $[B_{12}Br_{10}(H_2O)_2]^{-\bullet}$, with the distance between attractor 94 and oxygen nucleus of 0.89 Å being the smallest possible. This unexpected five-fold basin pattern could be related to the strong Lewis acidity of the naked boron atom, which might be inducing a strong polarization in the attached water moiety, in a similar fashion to a previous report of basin attractors at non-intuitive positions due to the polar/ionic character of the P–O bond in H_3PO.[45] This hypothetical strong polarization should be enhanced by the iodine substituents, or otherwise we would see the same behavior for the brominated species. This is by no means an in-depth study of the chemical bonding environment of the water moieties within these modified dodecaborate ions; further studies should be conducted, but our results suggest interesting differences between the bromine- and iodine-substituted ions. Spatial coordinates and detailed information for all the ELF attractors and basins identified in this work are provided in Section S5 of the SI.

In summary, we present pathways by which both $[B_{12}Br_{10}]^{-\bullet}$ and $[B_{12}I_{10}]^{-\bullet}$ can produce a first H_2 molecule spontaneously by mechanistic steps that can essentially be regarded as barrierless. Unfortunately, the subsequent reaction steps necessary to regenerate the original dodecaborate clusters with two uncoordinated boron atoms have a non-negligible energetic cost. However, this work demonstrates the potential to tune the reactivity of modified boron clusters to generate hydrogen *via* water splitting, which could pave the way for further studies exploring this concept. Additionally, our calculations showed different bonding environments for the water moieties in the bromine and iodine substituted species. The practical consequence of this for the hydrogen generation scheme we are proposing is that the hypothesized strong polarization of water moieties within the iodine-substituted system, compared to the brominated system, could be responsible for lowering the energy barrier for the hydrogen generation step on the mechanisms described in Fig. 4 and 5. Of course, further work is needed to test this hypothesis.

4 Conclusions

In this study, we have demonstrated that appropriately functionalized *closo*-dodecaborate anions ($[B_{12}Br_{10}]^{-\bullet}$ and $[B_{12}I_{10}]^{-\bullet}$) can promote spontaneous molecular hydrogen production from water under ambient conditions. The results establish that selective modification of the boron cluster framework can modulate the cluster's reactivity, enabling hydrogen release in the absence of external catalysts, photochemical activation, or an applied electrochemical potential. These findings expand the chemical utility of boron clusters by identifying a molecular-level pathway for water activation. Moreover, they underscore the potential of dodecaborate-based systems as tunable platforms for hydrogen generation, with possible implications for future energy-relevant material design. Additionally, our calculations indicate very distinct bonding environments for the water moieties in the brominated and iodinated dodecaborate species. This difference may influence the proposed hydrogen generation pathway, but further investigations are necessary to fully understand this aspect.

Conflicts of interest

There are no conflicts to declare.

Data availability

The data supporting this article have been included as part of the supplementary information (SI). Supplementary information is available. See DOI: https://doi.org/10.1039/d5cp04576b.

Acknowledgements

This work was supported by the U.S. Department of Energy, Office of Basic Energy Sciences, Division of Materials Sciences and Engineering under Award DE-FG02-96ER45579. HALP acknowledges the support of the U.S. Army Research Office through grant W911NF-23-1-0196. High Performance Computing resources provided by the High Performance Research Computing (HPRC) Core Facility at Virginia Commonwealth

University (https://chipc.vcu.edu) were used for conducting the research reported in this work.

References

1 T. Ohta, *Solar-Hydrogen Energy Systems*, Pergamon, 1979, pp. 25–33.
2 I. Dincer and C. Acar, *Int. J. Hydrogen Energy*, 2015, **40**, 11094–11111.
3 C. E. Housecroft and A. G. Sharpe, *Inorganic Chemistry*, Pearson Education Limited, Harlow, England, 5th edn, 2018.
4 I. Tiritiris and T. Schleid, *Z. Anorg. Allg. Chem.*, 2004, **630**, 1555–1563.
5 D. V. Peryshkov, A. A. Popov and S. H. Strauss, *J. Am. Chem. Soc.*, 2009, **131**, 18393–18403.
6 V. Geis, K. Guttsche, C. Knapp, H. Scherer and R. Uzun, *Dalton Trans.*, 2009, 2687–2694.
7 M. Mayer, V. van Lessen, M. Rohdenburg, G.-L. Hou, Z. Yang, R. M. Exner, E. ApràÃ, V. A. Azov, S. Grabowsky, S. S. Xantheas, K. R. Asmis, X.-B. Wang, C. Jenne and J. Warneke, *Proc. Natl. Acad. Sci. U. S. A.*, 2019, **116**, 8167–8172.
8 A. Avelar, F. Tham and C. Reed, *Angew. Chem., Int. Ed.*, 2009, **48**, 3491–3493.
9 C. Knapp, *Comprehensive Inorganic Chemistry II*, Elsevier, Amsterdam, end edn, 2013, pp. 651–679.
10 M. Rohdenburg, M. Mayer, M. Grellmann, C. Jenne, T. Borrmann, F. Kleemiss, V. A. Azov, K. R. Asmis, S. Grabowsky and J. Warneke, *Angew. Chem., Int. Ed.*, 2017, **56**, 7980–7985.
11 J. Warneke, T. Dülcks, C. Knapp and D. Gabel, *Phys. Chem. Chem. Phys.*, 2011, **13**, 5712–5721.
12 J. Warneke, *Int. J. Mass Spectrom.*, 2024, **496**, 117169.
13 P. Farràs, N. Vankova, L. L. Zeonjuk, J. Warneke, T. Dülcks, T. Heine, C. Viàñas, F. Teixidor and D. Gabel, *Chem. – Eur. J.*, 2012, **18**, 13208–13212.
14 H. Fang, D. Deepika and P. Jena, *J. Chem. Phys.*, 2021, **155**, 014304.
15 M. E. Kilic and P. Jena, *J. Phys. Chem. Lett.*, 2023, **14**, 8697–8701.
16 M. E. Kilic and P. Jena, *J. Phys. Chem. A*, 2024, **128**, 1993–2002.
17 M. Frisch, G. Trucks, H. Schlegel, G. Scuseria, M. Robb, J. Cheeseman, G. Scalmani, V. Barone, B. Mennucci and G. Petersson, *et al.*, *Gaussian 16 Rev. C.01*, Gaussian, Inc., Wallingford, CT, 2016.
18 A. D. Becke, *J. Chem. Phys.*, 1993, **98**, 5648–5652.
19 C. Lee, W. Yang and R. G. Parr, *Phys. Rev. B: Condens. Matter Mater. Phys.*, 1988, **37**, 785–789.
20 A. Bergner, M. Dolg, W. Kuechle, H. Stoll and H. Preuss, *Mol. Phys.*, 1993, **80**, 1431–1441.
21 W. J. Hehre, R. Ditchfield and J. A. Pople, *J. Chem. Phys.*, 1972, **56**, 2257–2261.
22 P. C. Hariharan and J. A. Pople, *Theor. Chim. Acta*, 1973, **28**, 213–222.
23 R. A. Kendall, T. H. J. Dunning and R. J. Harrison, *J. Chem. Phys.*, 1992, **96**, 6796–6806.
24 S. Grimme, S. Ehrlich and L. Goerigk, *J. Comput. Chem.*, 2011, **32**, 1456–1465.
25 C. Peng, P. Y. Ayala, H. B. Schlegel and M. J. Frisch, *J. Comput. Chem.*, 1996, **17**, 49–56.
26 V. Ásgeirsson, B. O. Birgisson, R. Bjornsson, U. Becker, F. Neese, C. Riplinger and H. Jónsson, *J. Chem. Theory Comput.*, 2021, **17**, 4929–4945.
27 F. Neese, *Wiley Interdiscip. Rev.: Comput. Mol. Sci.*, 2025, **15**, e70019.
28 S. Grimme, J. G. Brandenburg, C. Bannwarth and A. Hansen, *J. Chem. Phys.*, 2015, **143**, 054107.
29 T. Lu and F. Chen, *J. Comput. Chem.*, 2012, **33**, 580–592.
30 R. G. Parr and W. Yang, *J. Am. Chem. Soc.*, 1984, **106**, 4049–4050.
31 A. J. Frank, *Introduction to computational chemistry*, 3rd edn, 2017.
32 W. Yang and W. J. Mortier, *J. Am. Chem. Soc.*, 1986, **108**, 5708–5711.
33 B. Wang, C. Rong, P. K. Chattaraj and S. Liu, *Theor. Chem. Acc.*, 2019, **138**, 1–9.
34 J. Warneke, M. Mayer, M. Rohdenburg, X. Ma, J. K. Y. Liu, M. Grellmann, S. Debnath, V. A. Azov, E. Apra, R. P. Young, C. Jenne, G. E. Johnson, H. I. Kenttämaa, K. R. Asmis and J. Laskin, *Proc. Natl. Acad. Sci. U. S. A.*, 2020, **117**, 23374–23379.
35 X.-B. Wang, C.-F. Ding and L.-S. Wang, *Phys. Rev. Lett.*, 1998, **81**, 3351–3354.
36 A. D. Becke, *Phys. Rev. A: At., Mol., Opt. Phys.*, 1988, **38**, 3098–3100.
37 J. P. Perdew, *Phys. Rev. B: Condens. Matter Mater. Phys.*, 1986, **33**, 8822–8824.
38 E. van Lenthe, J. G. Snijders and E. J. Baerends, *J. Chem. Phys.*, 1996, **105**, 6505–6516.
39 J. Ochterski, *Thermochem. Gaussian*, 2000, 1–19.
40 F. S. Brigiano, Y. Jeanvoine, A. Largo and R. Spezia, *Astron. Astrophys.*, 2018, **610**, A26.
41 H. A. López Peña, J. M. Shusterman, C. Dalkiewicz, S. L. McPherson, C. Dunstan, K. Sangroula, K. U. Lao and K. M. Tibbetts, *J. Phys. Chem. A*, 2024, **128**, 1634–1645.
42 A. D. Becke and K. E. Edgecombe, *J. Chem. Phys.*, 1990, **92**, 5397–5403.
43 B. Silvi and A. Savin, *Nature*, 1994, **371**, 683–686.
44 B. Silvi and R. J. Gillespie, *The Quantum Theory of Atoms in Molecules: From Solid State to DNA and Drug Design*, Wiley-VCH, Weinheim, Germany, 2007, pp. 141–162.
45 D. B. Chesnut and A. Savin, *J. Am. Chem. Soc.*, 1999, **121**, 2335–2336.